

Tumor microenvironment-responsive self-assembly of barium titanate nanoparticles with enhanced piezoelectric catalysis capabilities for efficient tumor therapy



Zhuo Xiang ^a, Lingling Xu ^{b,c,d}, Yizhu Shan ^{b,c}, Xi Cui ^{b,c}, Bojing Shi ^{b,e}, Yuan Xi ^{b,f}, Panxing Ren ^{b,c}, Xuemei Zheng ^g, Chaochao Zhao ^{h,***}, Dan Luo ^{b,c,**}, Zhou Li ^{a,b,c,*}

^a Center on Nanoenergy Research, School of Physical Science & Technology, Guangxi University, Nanning, 530004, China

^b Beijing Institute of Nanoenergy and Nanosystems, Chinese Academy of Sciences, Beijing, 101400, China

^c School of Nanoscience and Technology, University of Chinese Academy of Sciences, Beijing, 100049, China

^d CAS Key Laboratory for Biomedical Effects of Nanomaterials and Nanosafety & CAS Center for Excellence in Nanoscience, National Center for Nanoscience and Technology of China, Beijing, 100190, China

^e School of Biological Science and Medical Engineering, Beihang University, Beijing, 100191, China

^f Beijing Advanced Innovation Centre for Biomedical Engineering, Key Laboratory for Biomechanics and Mechanobiology of Ministry of Education, School of Biological Science and Medical Engineering, School of Engineering Medicine, Beihang University, Beijing, 100191, China

^g College of Chemistry and Chemical Engineering, Center on Nanoenergy Research, Guangxi University, Nanning, 530004, China

^h Department of Biomedical Engineering, School of Medicine, Foshan University, Foshan, 528225, China

ARTICLE INFO

Keywords:

Self-assembly

Piezoelectric catalysis

Tumor microenvironment response

Sonodynamic therapy

ABSTRACT

Catalytic therapy based on piezoelectric nanoparticles has become one of the effective strategies to eliminate tumors. However, it is still a challenge to improve the tumor delivery efficiency of piezoelectric nanoparticles, so that they can penetrate normal tissues while specifically aggregating at tumor sites and subsequently generating large amounts of reactive oxygen species (ROS) to achieve precise and efficient tumor clearance. In the present study, we successfully fabricated tumor microenvironment-responsive assembled barium titanate nanoparticles (tma-BTO NPs): in the neutral pH environment of normal tissues, tma-BTO NPs were monodisperse and possessed the ability to cross the intercellular space; whereas, the acidic environment of the tumor triggered the self-assembly of tma-BTO NPs to form submicron-scale aggregates, and deposited in the tumor microenvironment. The self-assembled tma-BTO NPs not only caused mechanical damage to tumor cells; more interestingly, they also exhibited enhanced piezoelectric catalytic efficiency and produced more ROS than monodisperse nanoparticles under ultrasonic excitation, attributed to the mutual extrusion of neighboring particles within the confined space of the assembly. tma-BTO NPs exhibited differential cytotoxicity against tumor cells and normal cells, and the stronger piezoelectric catalysis and mechanical damage induced by the assemblies resulted in significant apoptosis of mouse breast cancer cells (4T1); while there was little damage to mouse embryo osteoblast precursor cells (MC3T3-E1) under the same treatment conditions. Animal experiments confirmed that peritumoral injection of tma-BTO NPs combined with ultrasound therapy can effectively inhibit tumor progression non-invasively. The tumor microenvironment-responsive self-assembly strategy opens up new perspectives for future precise piezoelectric-catalyzed tumor therapy.

1. Introduction

Cancer is a malignant disease with high morbidity and mortality,

threatening human health [1,2]. The vigorous development of nanotechnology allows for more efficient, safe, and precise tumor treatment strategies [3,4]. Nanomedicine not only includes nanocarriers that

Peer review under responsibility of KeAi Communications Co., Ltd.

* Corresponding author. Center on Nanoenergy Research, School of Physical Science & Technology, Guangxi University, Nanning, 530004, China.

** Corresponding author. Beijing Institute of Nanoenergy and Nanosystems, Chinese Academy of Sciences, Beijing, 101400, China.

*** Corresponding author.

E-mail addresses: zhaochaochao@fosc.edu.cn (C. Zhao), luodan@binn.cas.cn (D. Luo), zli@binn.cas.cn (Z. Li).

<https://doi.org/10.1016/j.bioactmat.2023.11.004>

Received 8 June 2023; Received in revised form 8 October 2023; Accepted 10 November 2023

Available online 20 November 2023

2452-199X/© 2023 The Authors. Publishing services by Elsevier B.V. on behalf of KeAi Communications Co. Ltd. This is an open access article under the CC BY-NC-ND license (<http://creativecommons.org/licenses/by-nc-nd/4.0/>).

deliver small molecule compounds, proteins, and nucleic acids precisely to tumor sites, but also covers functional materials that cause tumor cell damage by triggering *in situ* catalytic reactions [5–7]. Among many catalytic reactions, the efficient generation of ROS has become one of the representative strategies for tumor treatment. ROS themselves are oxygen metabolites that accompany cellular activity, and the high local concentration of ROS caused by catalytic reactions can lead to protein/lipid oxidation, DNA strand breaks, and base damage [8,9]. To date, many catalytic strategies have been proposed to generate large amounts of ROS for cancer therapy, including photodynamic therapy (PDT) [10–13], chemodynamic therapy (CDT) [14–16], and sonodynamic therapy (SDT) [17,18]. As one of them, the SDT strategy mainly uses sonosensitizers to convert the mechanical energy of ultrasound into chemical energy [19,20]. Benefiting from the high tissue penetration and controllable low-level tissue damage of ultrasound as an external stimulus source, the SDT strategy has strong prospects for clinical translation, and the development of high-performance sonosensitizers has become the key to the successful implementation of SDT.

Piezoelectric semiconductor nanomaterials are ideal sound sensitizers [21,22]. The periodic mechanical stress of ultrasound will cause the deformation of the piezoelectric material and generate polarization inside the crystal, thereby effectively inducing the separation of electrons and holes at the interface and finally catalyzing the generation of ROS [23–26]. To date, a series of piezoelectric materials such as zinc oxide (ZnO) [27,28], boron nitride (BN) [29,30], and barium titanate (BTO) [31,32] have realized the application in biomedicine; among them, BTO NPs have become widely used sonosensitizers in SDT due to their good biocompatibility, low cytotoxicity, and strong piezoelectricity [33–36]. However, SDT strategies based on BTO NPs still face difficulties in the selectivity of delivery and precision of treatment. Although large NPs (~200 nm) have strong piezoelectric catalytic activity, they are easily phagocytized by macrophages and normal tissue cells, making them difficult to transport from the peritumoral to tumor tissue. However, smaller nanoparticles are prone to exocytosis while being endocytosed by cells, making it difficult to achieve specific intratumoral accumulation [37,38]. Since the cytotoxicity of ROS to normal cells and tumor cells is indifferent, the lack of specific delivery to tumor sites will lead to poor therapeutic effects and raise biosafety concerns. Therefore, developing a piezoelectric nanoparticle that responds to the tumor environment to achieve specific aggregation at the tumor site and exert a strong piezoelectric catalytic effect is the key to achieving efficient SDT.

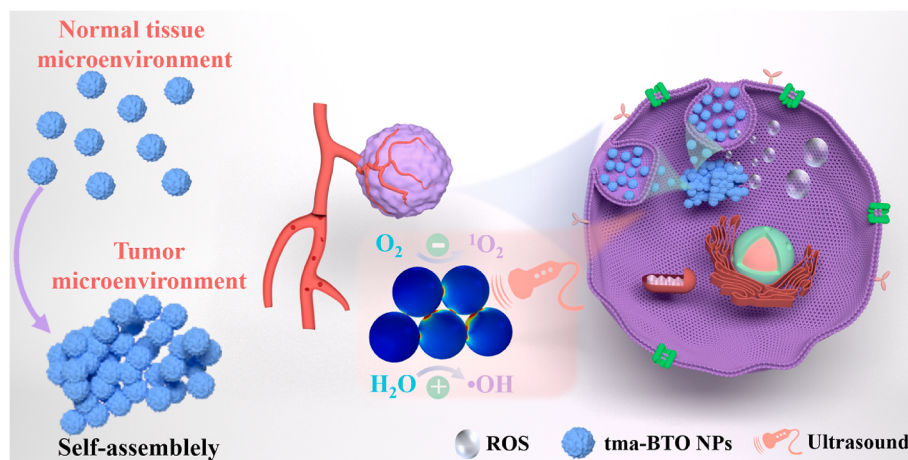
Herein, we synthesized uniform small-sized BTO NPs with a diameter of 18.15 ± 3.64 nm using the solvothermal method. Inspired by the acidic tumor microenvironment [39,40], pH-responsive ligands were synthesized and anchored to the surface of BTO NPs to form tumor

microenvironment-responsive assembled BTO nanoparticles (tma-BTO NPs), in which the pH-responsive ligands could protonate part of the negative charges to positive charges in the acidic tumor microenvironment and induce the self-assembly of BTO NPs via Coulomb forces. After co-culture with 4T1 cells for 24 h, the diameter of the assemble tma-BTO NPs reached submicron scale, which caused mechanical damage to 4T1 cells. More importantly, the assembled tma-BTO NPs showed stronger piezoelectric catalytic efficiency than monodisperse BTO NPs under the excitation of ultrasonic waves, resulting in more ROS generation and ultimately triggering more apoptosis of 4T1 cells (Scheme 1). Mechanistically, the enhanced piezoelectric catalytic effect can be ascribed to the mutual extrusion of neighboring particles within the confined space of the assembly. In contrast, tma-BTO NPs seldom aggregated and remained well dispersed after co-cultivation with MC3T3-E1 cells for 24 h, maintaining high biocompatibility to normal tissues due to their ability to cross the intercellular space. In animal experiments, 4T1-tumor-bearing mice achieved excellent therapeutic performance with minimal solid tumor after the treatment with tma-BTO NPs under ultrasound excitation. These findings are particularly valuable for the development of novel sonosensitizers that could enable precise therapy.

2. Results and discussion

2.1. Synthesis and characterization of tma-BTO NPs

Hydrophobic BTO NPs were successfully prepared by a modified hydrothermal synthesis. Transmission electron microscope (TEM) showed that the BTO NPs were approximately spherical with an average diameter of 18.15 ± 3.64 nm (Fig. 1a). High-resolution transmission electron microscopy (HRTEM) revealed that the as-prepared BTO NP possessed a single-crystalline structure, and well-defined lattice fringes with interplanar distances of 0.28 nm inferred to the (110) planes of BTO (Fig. 1b). The energy-dispersive X-ray spectroscopy (EDX) elemental mapping well defined the Ba and Ti elements, confirming the formation of BTO nanomaterials (Fig. S1). The selected area electron diffraction (SAED) pattern further demonstrated characteristic crystallographic orientations of BTO NPs with diffraction spots indexed to the (100), (110), (200), (211), (220) and (310) planes (Fig. 1c). The atomic force microscopy (AFM) results showed that the height of BTO NPs was 22.05 ± 4.62 nm, slightly larger than the TEM results, attributed to the oleic acid ligands encapsulated on the surface of the NPs (Fig. 1d). To further investigate the piezoelectricity, piezoresponse force microscopy (PFM) was used to scan BTO NPs thermal deposited on the surface of conductive silicon substrate. Typical butterfly amplitudes were observed when a 20 V AC voltage was applied (Fig. 1e). On the phase chart, the clear hysteresis loop of BTO NPs plotted 180° phase switching (Fig. 1f).



Scheme 1. Schematic illustration of enhanced piezocatalytic performance based on self-assembly tma-BTO NPs under US stimuli.

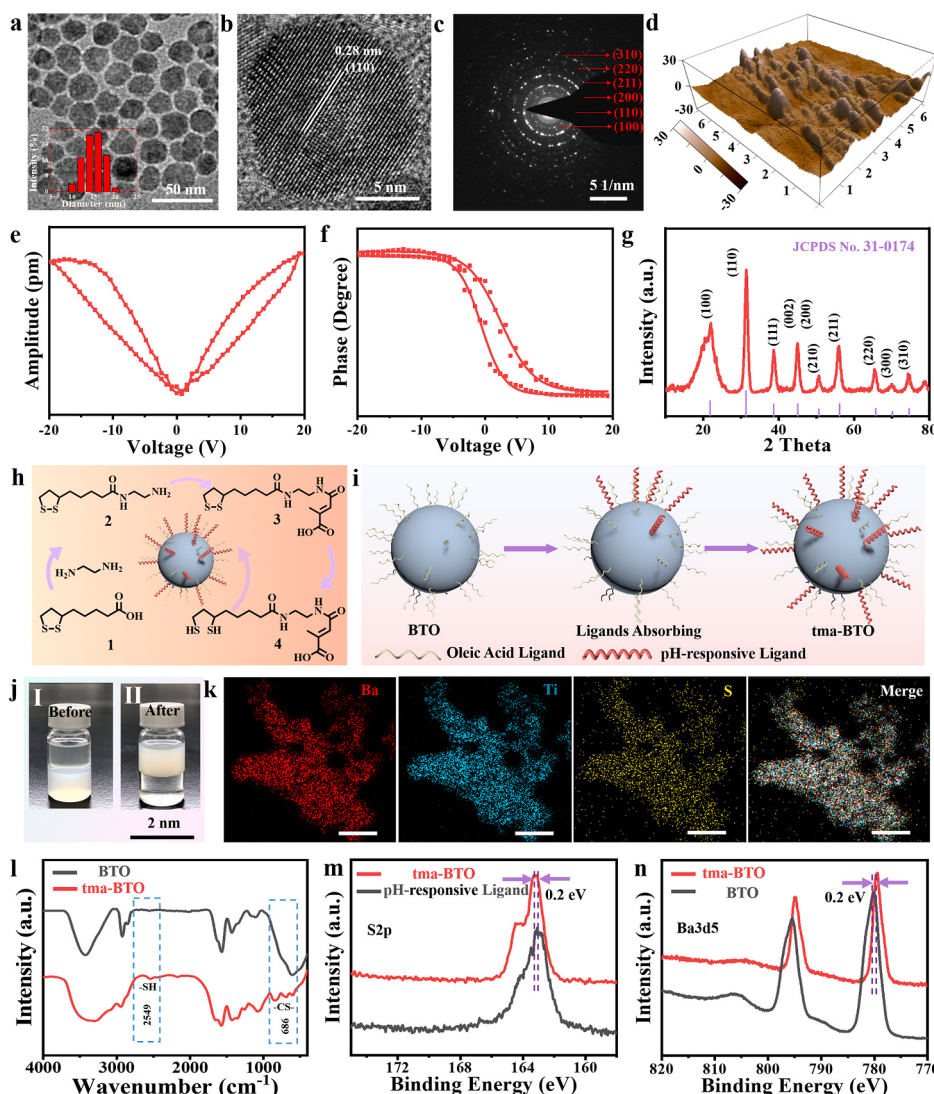


Fig. 1. Morphological and structural characterizations of BTO. (a) TEM image, (b) HRTEM image, (c) and selected area electron diffraction pattern. (d) AFM image of BTO binding to a conductive silicon substrate. (e) Amplitude curve, (f) and piezoresponse phase curve of BTO NPs. (g) XRD pattern of BTO. (h) The process diagram of preparation pH-responsive ligand. (i) The schematic diagram of pH-responsive ligand coating on the surface of BTO NPs, (j) and the photos recording the formation of tma-BTO transferring from chloroform phase to water phase (top: water; bottom: chloroform). (k) EDX elemental mapping of tma-BTO (scale bar: 200 nm). (l) FTIR spectra of BTO and tma-BTO. (m) S2p XPS spectrum of tma-BTO and pH-responsive ligand, (n) Ba3d5 XPS spectrum of tma-BTO and BTO.

demonstrating the excellent piezoelectric response and also proved their ferroelectric domains. The PFM images showed the height, magnitude, and phase of BTO NPs, respectively (Fig. S2). The variations that appear in the PFM signal might arise from the fact that the BTO NPs were composed of multiple stochastically oriented ferroelectric domains. The crystal structure of BTO NPs was further measured by X-ray diffraction (XRD), which revealed nearly identical lattice parameters to tetragonal barium titanate (JCPDS No. 31–0174) (Fig. 1g, Fig. S3a). From Tauc plots of UV-visible absorption spectrum, it can be seen that the band gap of the as-prepared BTO NPs was ~1.36 eV (Fig. S3b).

The synthesis of functionalized ligands and their modification on the surface of nanoparticles is the key for BTO to achieve the tumor environment response. In this research, (\pm)- α -lipoic acid was sequentially reacted with ethylenediamine and citraconic anhydride, respectively (Fig. 1h). The newly formed 4-((2-(5-(1,2-dithiolan-3-yl)pentanamido)ethyl) amino)-2-methyl-4-oxobut-2-enoic acid (^1H NMR was shown in Fig. S4) was reduced with sodium borohydride via ring-opening reaction in aqueous solution to obtain the final product 4-((2-(6,8-dimercaptooctanamido)ethyl)amino)-2-methyl-4-oxobut-2-enoic acid, which presented a pH-responsiveness by through protonation in the weakly

acidic environment. The prepared pH-responsive ligands, 4-((2-(6,8-dimercaptooctanamido)ethyl)amino)-2-methyl-4-oxobut-2-enoic acid, could be adsorbed on the surface of BTO NPs through van der Waals forces and hydrogen bonds (Fig. 1i). The coating reaction of pH-responsive molecules on the surface of BTO NPs occurred at the interface of chloroform and water, where the hydrophobic BTO NPs were dispersed in the chloroform phase and the pH-responsive ligands dissolved in the aqueous phase. By vigorous stirring, BTO gradually transferred from the bottom chloroform phase to the upper aqueous phase to form tma-BTO NPs (Fig. 1j). tma-BTO NPs dispersed in neutral aqueous solution possessed good dispersion, and the coating of ligands did not change the original size and morphology of BTO NPs (Fig. S5). We confirmed the presence of pH-responsive ligands in tma-BTO by ESI mass spectrometry. As shown in Fig. S6, the molecular ion peak and fragment peak of the pH-responsive ligand can be observed regardless of the positive ion mode or the negative ion mode. The FTIR (Fourier transform infrared) spectrum results showed that tma-BTO NPs exhibited absorption peaks at $\sim 2550 \text{ cm}^{-1}$, $\sim 680 \text{ cm}^{-1}$, which correspond to the stretching vibration peaks of sulfur-hydrogen bonds and carbon-sulfur bonds respectively (Fig. 1l) [41,42]. The X-ray photoelectron

spectroscopy analysis (XPS) further confirmed the ligand coating on the surface of BTO NPs. As shown in Fig. S7, peaks corresponding to Ba, O, Ti, N and S appeared in the tma-BTO spectrum, while N and S peaks were not observed in the BTO group. EDX elemental analysis is also consistent with the results of XPS. Ba, Ti and S elements were uniformly distributed in tma-BTO NPs, while sulfur and nitrogen elements were not present in hydrophobic BTO NPs (Fig. 1k, Fig. S8). Interestingly, we also found evidence that bidentate thiol ligands may be chemically adsorbed on the BTO surface. The S 2p peak of the pH-responsive ligand monomer possessed a binding energy of 162.98 eV, while when it is anchored to the BTO surface, the S 2p peak was shifted by 0.2 eV to a higher binding energy of 163.18 eV (Fig. 1m). On the contrary, in the Ba 3d5 spectrum, the binding energy decreased by 0.2 eV from 779.73 eV to 779.58 eV after ligand coating (Fig. 1n). Moreover, the characteristic S2p peaks of

tma-BTO were observed at 164.23 eV and 163.18 eV, indexing to S2p_{1/2} and S2p_{3/2}, respectively (Fig. S9). More importantly, a peak located at 164.68 eV can be attributed to sulfur compounds. In comparison, the XPS spectrum of the pH-responsive ligand showed only two peaks. In addition, we also performed thermogravimetric analysis (TGA) and differential thermal analysis (DTA) on BTO and tma-BTO under N₂ atmosphere (Fig. S10). BTO lost 9.94 % of its mass at 900° due to the pyrolysis of the oleic acid ligand; in comparison, the weight loss of tma-BTO at the same temperature reached 18.58 %; in addition, the DTA curves of the two also exist significant difference. The above results have consistently confirmed that pH-responsive ligands are successfully coated on the BTO surface.

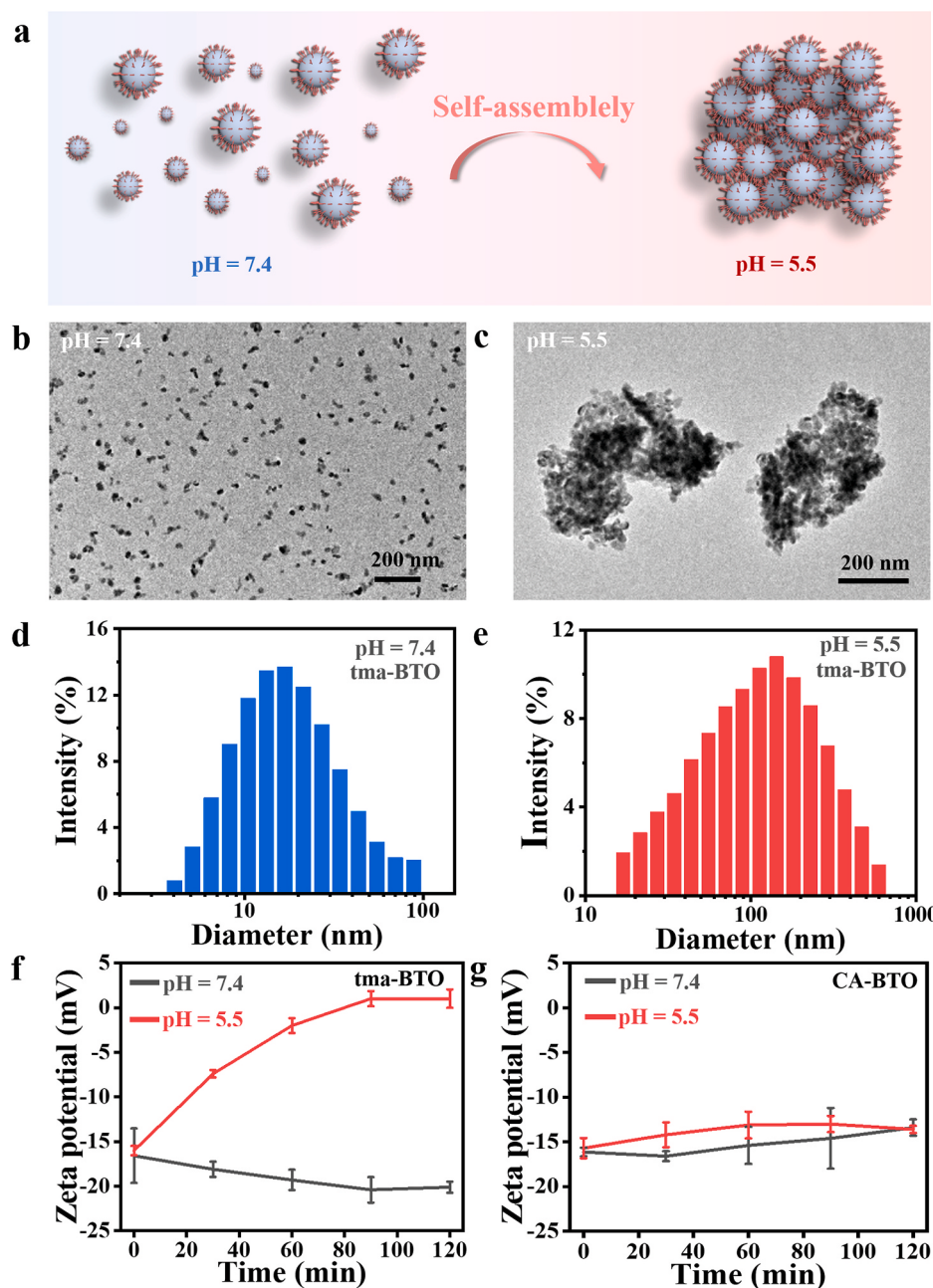


Fig. 2. (a) The aggregation of self-assembly tma-BTO NPs from pH 7.4 to pH 5.5 condition. TEM images of (b) the monodispersed tma-BTO NPs and (c) the aggregated tma-BTO NPs. The hydrodynamic size distribution of tma-BTO NPs at (d) pH 5.5 and (e) pH 7.4 condition. Zeta-potential of (f) tma-BTO NPs and (g) CA-BTO with time-dependent variations.

2.2. The pH-responsive aggregation ability of tma-BTO NPs

The as-prepared tma-BTO NPs exhibit pH-responsive self-assembly properties (Fig. 2a). TEM results showed that the tma-BTO NPs dispersed in a neutral solution simulating normal body fluid (pH = 7.4) hardly agglomerated (Fig. 2b); while in the weakly acidic solution simulating the tumor microenvironment (pH = 5.5), the same concentration of tma-BTO NPs would assemble to form aggregates with a size of ~200 nm (Fig. 2c), which might attribute to the fact that the acidic environment partially converted negative charges of the ligands to positive charges and triggered the assembly reaction induced by Coulomb forces (Fig. S11) [43,44]. The zeta potential and hydrodynamic size of tma-BTO NPs in different pH environments were further tested by using dynamic light scattering (DLS). Consistent with TEM, the tma-BTO NPs are well dispersed in a neutral environment with a pH value of 7.4 (Fig. 2d); while they are clearly aggregated in a mild acidic solution with a pH value of 5.5 (Fig. 2e). The self-assembly kinetics of tma-BTO NPs was further monitored by the change of zeta potential. The onset zeta potential of tma-BTO NPs in weakly acidic environment was slightly higher than that in neutral environment, ascribing to the instantaneous protonation of the ligands. We observed that the zeta potential of tma-BTO NPs gradually increased from -15 mV to 0 mV within 120 min in a solution at pH 5.5, which was attributed to the shielding of the

internal particle potential inside the Coulomb force-induced self-assembled structure. In contrast, the zeta potential of tma-BTO NPs remained almost unchanged in a neutral environment (Fig. 2f). We further used citrate acid as a ligand to fabricate pH-unresponsive water-soluble BTO NPs (CA-BTO), whose potential remained almost constant in both weakly acidic and neutral environments (Fig. 2g). It is worth mentioning that when tma-BTO NPs and CA-BTO NPs were dispersed in DMEM (Dulbecco's Modified Eagle Medium), phosphate buffer (pH = 7.4), and citric acid-disodium hydrogen phosphate buffer for 12 h, all groups showed a high degree of dispersion with little change in their hydrodynamic diameters. The above experiments confirmed that tma-BTO NPs and CA-BTO NPs possessed good colloidal properties, and the specific assembly of tma-BTO NPs only occurs in acidic media (Figs. S12 and S13). In addition, XRD results showed that the crystal structure of self-assembled tma-BTO NPs in weakly acidic media is consistent with that of monodispersed nanoparticles in neutral pH media (Fig. S14).

2.3. ROS generation ability of tma-BTO

The piezoelectricity of BTO originates from the asymmetric shift of dipole moment, which is the main requisite for piezocatalytic performance. The ultrasonic cavitation effect acted as a stress source loaded on

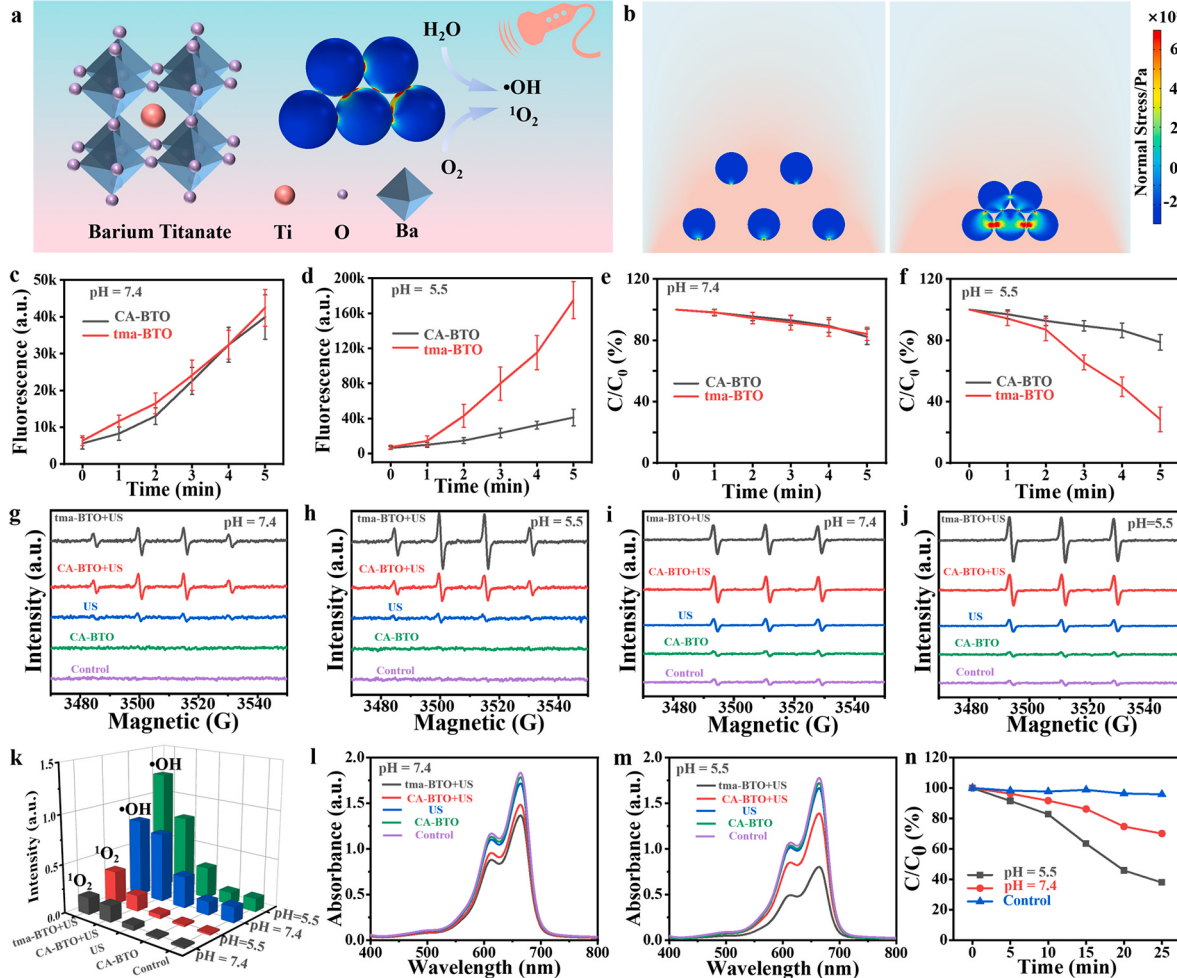


Fig. 3. Piezocatalytic performance of tma-BTO and CA-BTO under US irradiation. (a) Schematic diagram illustrating the generation of $\bullet\text{OH}$ and $^1\text{O}_2$ based on US triggering piezoelectric effect. (b) 2D FEM simulations of the monodispersed BTO and the aggregated BTO by ultrasonic pressure. TA for the detection $\bullet\text{OH}$ with the increased US irradiation time, the fluorescence intensity of samples (c) at pH 7.4 and (d) pH 5.5 solution ($n = 4$). DPBF for the detection of $^1\text{O}_2$ with the increased US irradiation time, the absorbance intensity of samples (e) at pH 7.4 and (f) pH 5.5 solution ($n = 4$). ESR spectra of $^1\text{O}_2$ (g) at pH 7.4 and (h) pH 5.5 solution trapped by TEMP. (k) The ESR data summarized in a 3D graph. UV-vis absorption spectrum of MB aqueous solution (l) at pH 7.4 and (m) at pH 5.5. (n) MB degradation curves with increasing US irradiation time.

the BTO NPs, which leaded to the separation of electrons and holes, and effectively catalyzed the generation of ROS (Fig. 3a). Interestingly, finite element analysis (FEA) revealed that the assembled tma-BTO NPs were subjected to much larger forces than monodisperse nanoparticles, which was due to the fact that the assembled particles were not only stressed by ultrasonic waves, but also to mutual compression of neighboring particles caused by the tightly arranged structure inside the assemblies (Fig. 3b). This force-enhanced effect induced by the assembled structure predicts stronger piezoelectric catalytic performance with more ROS generation.

To evaluate the ROS generation, hydroxyl radical ($\bullet\text{OH}$) and singlet oxygen (${}^1\text{O}_2$) were detected by using terephthalic acid (TA) and 1,3-diphenylisobenzofuran (DPBF), respectively (Figs. S15 and S16)). According to previous reports, 1.0 MHz and 1.0 W/cm² are appropriate parameters for effectively triggering piezocatalysis and suitable for clinical research [45,46]. Under ultrasonic irradiation, the $\bullet\text{OH}$ generated by tma-BTO NPs will oxidize nonfluorescent TA and convert it into highly fluorescent 2-hydroxyterephthalic acid (HTA). With the prolongation of ultrasound time, the fluorescence emission of HTA at 426 nm gradually increased, indicating that the generation of $\bullet\text{OH}$ was time-dependent. Both the tma-BTO NPs and CA-BTO NPs exhibited similar fluorescence growth trends in the solution environment at pH 7.4 (Fig. 3c). In contrast, assembled tma-BTO NPs produced a stronger fluorescence signal under ultrasound in an environment with pH 5.5. After sonication for 5 min, the fluorescence intensity of the tma-BTO group was 4.26 times higher than that of the CA-BTO group, implying more $\bullet\text{OH}$ production (Fig. 3d). DPBF as a scavenger of ${}^1\text{O}_2$ can be degraded by ${}^1\text{O}_2$, which is suitable for investigating the variations of ${}^1\text{O}_2$. The absorption peak of DPBF at 411 nm decreased with increasing ultrasound time. Similar to the TA test, monodispersed tma-BTO NPs and CA-BTO NPs showed similar trends towards DPBF catalytic degradation at pH 7.4 (Fig. 3e). However, in the pH 5.5 environment, the absorption of DPBF in the tma-BTO group rapidly dropped to 28.40 % of the initial value after 5 min of ultrasonic irradiation, while the absorption of DPBF in the CA-BTO group could still maintain approximately 80 % of the initial value, indicating that the assembled tma-BTO NPs were also able to generate more ${}^1\text{O}_2$ (Fig. 3f). Taken together, the assembled tma-BTO NPs significantly improved the sonodynamic efficiency, which was consistent with the finite element analysis.

Electron spin resonance (ESR) as a classic and typical method was utilized for further ROS analysis. TEMP (2,2,6,6-Tetramethylpiperidine), a typical spin-trapping agent for capturing radical ${}^1\text{O}_2$ yielded 1:1:1 triple signal of the 2,2,6,6-tetramethyl-1-piperidinyloxy (TEMPO) in aqueous. The characteristic 1:2:2:1 quadruple signal of DMPO-OH• derived from the spin-trapping agent of DMPO (5,5-dimethyl-1-pyrroline-N-oxide) bounding to OH•. As shown in Fig. 3g and h, we tested the ESR spectra of tma-BTO NPs plus ultrasound stimulation group (tma-BTO + US), CA-BTO NPs plus ultrasound stimulation group (CA-BTO + US), ultrasound stimulation group (US), CA-BTO group, and the blank group in the environment of pH 5.5 and 7.4, separately. In the absence of ultrasound irradiation, no $\bullet\text{OH}$ signal was detected in CA-BTO and the blank group, indicating that US played a “switch” role for triggering the $\bullet\text{OH}$ generation. While in the pure US group, we hardly observed the typical $\bullet\text{OH}$ signal, confirming that only water without piezoelectric nanomaterials could hardly generate $\bullet\text{OH}$. At pH 7.4, there was no difference between the tma-BTO + US group and the CA-BTO + US group. However, at pH 5.5, the tma-BTO + US group with assembled state exhibited the strongest free radical signal (Fig. 3i). In addition, we also assessed ${}^1\text{O}_2$ production, and the trend of ${}^1\text{O}_2$ production among the groups was similar to that of $\bullet\text{OH}$ (Fig. 3j). Collectively, ESR tests yielded conclusions consistent with those of the ROS indicator: tma-BTO NPs assembled under acidic conditions exhibited stronger piezoelectric catalytic efficiency and induced more ROS production than monodisperse nanoparticles under ultrasonic excitation (Fig. 3k). The degradation of methylene blue (MB), a classic organic pollutant model compound, was used to further evaluate the piezocatalytic performance

of each group. The absorption peak of MB at 10 mg/L also showed no significant change in US, CA-BTO and blank groups. In the solution of pH 7.4, the tma-BTO + US group and the CA-BTO + US group had similar MB degradation ability. However, in the pH 5.5 solution, the degradation rate of the tma-BTO + US group (55.5 %) was over 2.2 times higher than that in the pH 7.4 (25.3 %) (Fig. 3l, 3m). The efficient dye degradation revealed that tma-BTO NPs were able to exhibit stronger oxidation ability in the acid tumor microenvironment.

2.4. Piezocatalysis effect-mediated *in vitro* cytotoxicity

To investigate the ability of tma-BTO NPs to selectively accumulate in the tumor microenvironment and effectively kill cancer cells through SDT, mouse breast cancer cells (4T1) were selected as the study model and normal cells (mouse embryo osteoblast precursor cells, MC3T3-E1) served as controls. The cytotoxicity of tma-BTO NPs and CA-BTO NPs after co-cultivation for 24 h was determined by CCK-8 kit. In the absence of ultrasound, both tma-BTO NPs and CA-BTO NPs maintained good biocompatibility with MC3T3-E1, and the cell viability reached 85.39 % of the initial value even at a high concentration of 500 µg/mL, indicating that the two types of BTO nanoparticles possessed negligible toxicity to normal cells. However, in 4T1 cells, tma-BTO NPs showed more significant cytotoxicity than CA-BTO NPs, which might be attributed to the cell damage caused by the responsive aggregation of tma-BTO NPs in the tumor microenvironment (Fig. 4a). In addition, we also evaluated the cell viability after long-term co-culture (48 h, 72 h) with tma-BTO NPs and CA-BTO NPs, and the trend was consistent with that of co-culture for 24 h (Fig. S17). Under ultrasonic irradiation, tma-BTO NPs significantly induced the apoptosis of 4T1 cells, and the cell viability dropped sharply to 16.73 % of the initial value at 200 µg/mL; while the damage to MC3T3-E1 cells was negligible under the same conditions. In contrast, CA-BTO NPs did not exhibit selective killing effects on tumor cells and had much lower therapeutic efficiency than that of tma-BTO NPs (Fig. 4b).

Optical microscopy images provided intuitive evidence revealing the effect of different extracellular matrices on the aggregation state of BTO NPs (Fig. 4c). After 24 h incubation with 4T1 cells, almost no significant aggregation of CA-BTO NPs occurred. It is worth pointing out that some CA-BTO NPs inevitably form tiny aggregate structures, which may be caused by the electrical attraction between nanoparticles and the charged protein in DMEM medium. In contrast, tma-BTO NPs formed submicron-scale assemblies in the tumor extracellular matrix. Both tma-BTO NPs and CA-BTO NPs showed negligible accumulation when cultured with MC3T3-E1 cells. The co-cultured cells (tma-BTO, 200 µg/mL) were further immobilized and sliced for TEM analysis (Fig. 4d). From the perspective of microstructure, TEM images showed that the assembled tma-BTO NPs were endocytosed by 4T1 cells and retained in the cytoplasm; while less tma-BTO NPs were retained in MC3T3-E1 cells, which was due to the small-sized nanoparticles were easily expelled from the cell by exocytosis.

Calcein AM/PI fluorescence probes were applied to visualize the therapeutic performance of the piezocatalytic effect (Fig. 4e). For 4T1 cells, strong red fluorescent signal (PI) in the tma-BTO + US group represented severe cytotoxicity to tumor cells. While in MC3T3-E1 cells, all groups presented strong green fluorescence signals (Calcein-AM), proving that tma-BTO NPs had little effect on normal cell viability. To confirm at the cellular level that the toxicity against tumor cells originates from the enhanced piezoelectric catalytic performance caused by the assembly of tma-BTO NPs, the 2',7'- dichlorofluorescein diacetate (DCFH-DA) was used to label generated ROS (Fig. 4f). Non-fluorescence DCFH-DA was rapidly oxidized by ROS to form green fluorescent 2',7'- dichlorofluorescein (DCF). A distinct green fluorescence signal was only observed in the tma-BTO + US group on 4T1 cells, demonstrating that tma-BTO NPs assembled in the tumor microenvironment efficiently generated ROS and eliminated tumor cells.

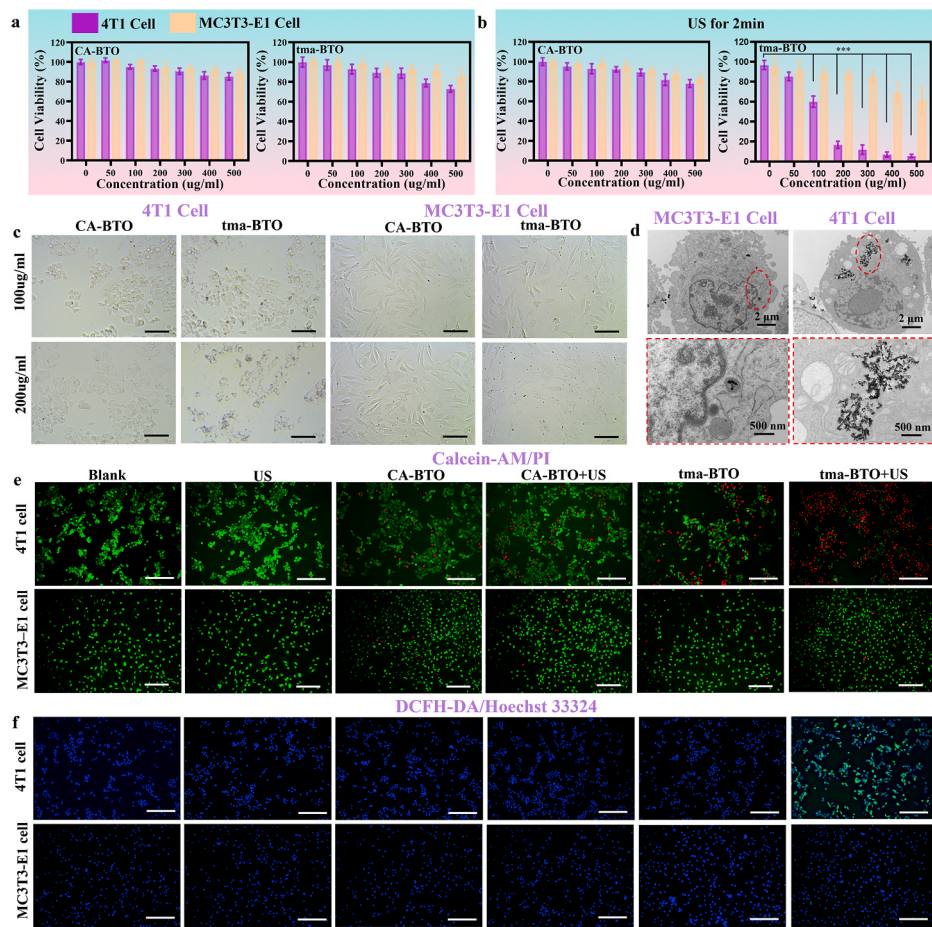


Fig. 4. *In vitro* therapeutic performance on 4T1 cells with various groups. (a) Cytotoxicity profiles of 4T1 cells or MC3T3-E1 cells after incubating with CA-BTO and tma-BTO for 24 h. (b) Cell viabilities after exposure to US irradiation (* $p < 0.05$, ** $p < 0.01$, *** $p < 0.001$). (c) Micrographs of 4T1 cells and MC3T3-E1 cells after incubating with CA-BTO or tma-BTO for 24 h (Scale bar = 100 μm), and (d) TEM images showing the intracellular location of tma-BTO aggregations. Confocal fluorescence images of 4T1 cells and MC3T3-E1 cells under US irradiation, (e) Calcein-AM/PI and (f) DCFH-DA/Hoechst 33324 fluorescence staining (Scale bar = 200 μm).

2.5. In vivo therapeutic performance of tma-BTO

Tumor-bearing mice were further used to evaluate the piezocatalytic therapeutic performance *in vivo* (Fig. 5a). 4T1 cells were implanted in BALB/c mice (the top of thighs) via subcutaneous injection. Like the cell experiments, the animal model was also divided into 6 groups with 6 mice in each group ($n = 6$), including: blank group, US group, CA-BTO group, tma-BTO group, CA-BTO + US group, and tma-BTO + US group. On day 7, BTO NPs solution (100 μl ; 2 mg/100 g mice body weight) was administered through peritumoral injection (the blank group was injected with an equal volume of normal saline), and ultrasound radiation (1.0 MHz, 1.0 W/cm², 50 % duty cycle, each time for 2 min, 3 times a day) was applied on the skin surface from day 8 to day 16 to trigger piezoelectric catalysis. From the perspective of tumor volume, the tma-BTO + US group showed apparent tumor inhibition, while the other groups still showed a tendency of tumor growth during therapeutic period (Fig. 5b). In addition, no significant changes in the body weight of the mice were observed during the treatment period, indicating the safety of the tma-BTO NPs-based therapeutic strategy (Fig. 5c). All mice were sacrificed on day 24, and the tumors were collected and weighed. There was no significant difference between the blank group, the US group and the CA-BTO group. Although the CA-BTO + US group could produce a certain amount of ROS, the lack of specific accumulation in the tumor microenvironment and the weak piezoelectric catalytic efficiency limited its tumor inhibitory effect. The tma-BTO group also showed some tumor suppressive effect, which might be

attributed to the mechanical damage caused by the assembly of NPs at the tumor site. The treatment effect of the tma-BTO + US group was overwhelming among all blank groups, and the average tumor weight in this group decreased by 83.5 % compared with the blank group, which was mainly attributed to the enhanced piezoelectric catalytic effect induced by self-assembly (Fig. 5d). In addition, as studied by Marino et al., piezoelectric stimulation can also induce cell cycle arrest and significantly reduce tumor cell proliferation by affecting the organization of mitotic spindles during mitosis [47–49]. The photos also show the size of solid tumors in different groups of mice after treatment (Fig. 5e and f), among which the tma-BTO + US group had the highest therapeutic performance with the smallest tumor volume.

Hematoxylin and eosin (H&E) staining can clearly visualize the microscopic morphology of sectioned tissue by inducing different refractive indices of cell nuclei and cytoplasm. H&E staining assays investigated the collected solid tumors to verify the therapeutic efficiency. Among six groups, US triggering tma-BTO achieved the highest tumor tissue damage, suggesting its excellent sonodynamic treatment. Proliferation-associated Ki-67 protein can be detected during all the active phases of the cell cycle but absent in resting cells, allowing assessment of tumor cell proliferation. Ki-67 assays were performed to further assess the level of tumor cell proliferation. Only the tma-BTO + US group showed barely positive nuclei, revealing excellent tumor inhibition. Similarly, terminal deoxynucleotidyl transferase (TdT)-mediated deoxyuridine triphosphate (dUTP) nick end labeling (TUNEL) staining assays associated with tumor cell apoptosis. We observed that

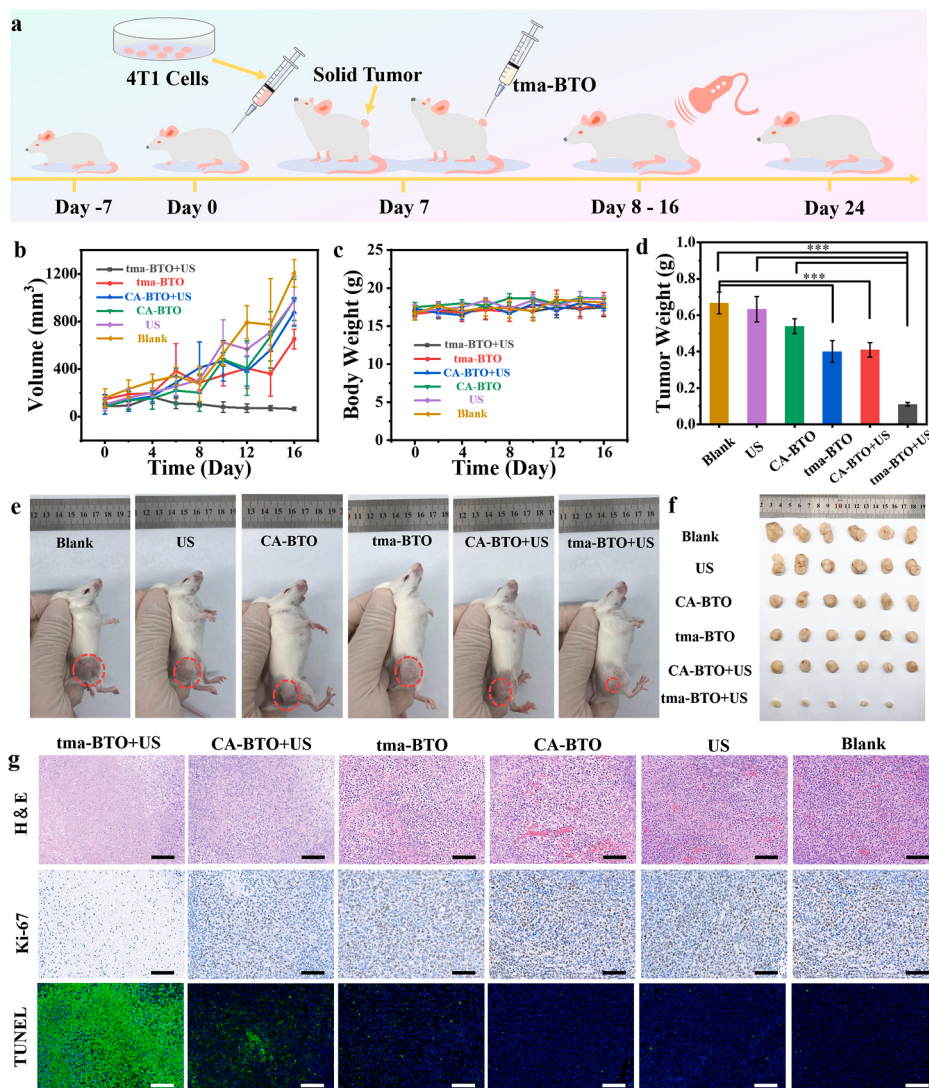


Fig. 5. *In vivo* therapeutic performance on solid tumor under US irradiation. (a) Schematic illustration of preparation and therapeutic process. (b) The tumor-growth curves from 0 to 16 days. (c) Average body weight change of 4T1-tumor-bearing mice. Data are presented as mean values \pm s.d. ($n = 6$). (d) Average weight of solid tumors on day 24. (e) Digital photos of 4T1-tumor-bearing mice and their tumor site, and (f) solid tumors on day 24. (g) H&E, Ki-67, and TUNEL staining assay of tumor slices on day 24 (Scale bar = 100 μ m). (* $p < 0.05$, ** $p < 0.01$, *** $p < 0.001$).

the tma-BTO + US group presented a stronger TUNEL fluorescence signal than the other groups, the results were consistent with H&E and Ki-67 assay (Fig. 5g), proving that US-triggering tma-BTO NPs were able to achieve high-efficient cancer therapy *in vivo*.

2.6. The biological safety evaluation of tumor therapy

After *in vivo* cancer therapy, blood from tumor-bearing mice was collected and used for biochemistry assay. As shown in Fig. 6a, inflammation-related indicators such as white blood cells (WBC), lymphocytes (LYM#), middle-sized cells (MID#), and granulocytes (GRA#) in the tma-BTO + US columns were significantly lower than those in the rest of the groups. The results revealed that piezocatalytic treatment could reduce the inflammatory environment of tumors by efficiently inducing tumor cell apoptosis. We also evaluated hepatic and renal function markers including blood urea nitrogen (BUN), creatinine (CREA), alanine (ALT), and aspartate aminotransferase (AST). There were no abnormal changes in all groups, demonstrating the safety of the piezocatalytic treatment (Fig. 6b). In addition, non-inflammatory related blood indicators, including red blood cells (RBCs), hemoglobin (HGB), hematocrit (HCT), mean corpuscular volume (MCV), mean

corpuscular hemoglobin (MCH), mean corpuscular hemoglobin concentration (MCHC), plateletcrit (PCT) and plaqua (PLT) were all within normal reference range (Fig. 6c). H&E staining further verified the potential damage to major organs (such as heart, liver, spleen, lung, and kidney). The results confirmed that the tma-BTO + US group was consistent with the blank group, and no obvious organ damage was observed (Fig. 6d).

3. Conclusion

In summary, we have prepared tma-BTO NPs to achieve selective killing against tumor cells. tma-BTO NPs exhibited responsive self-assembling properties in the tumor microenvironment; while maintaining a dispersed state in the normal extracellular matrix, which could minimize the negative effects associated with the mechanical damage and piezoelectric-catalyzed ROS on normal cells. Self-assembled tma-BTO NPs exhibited enhanced mechanical damage and piezoelectric catalytic efficiency to synergistically induce more apoptosis in 4T1 cells under ultrasound excitation. This work developed a new generation of smart sonosensitizers with tumor responsiveness to achieve efficient cancer therapy with attenuated side effects, opening up new

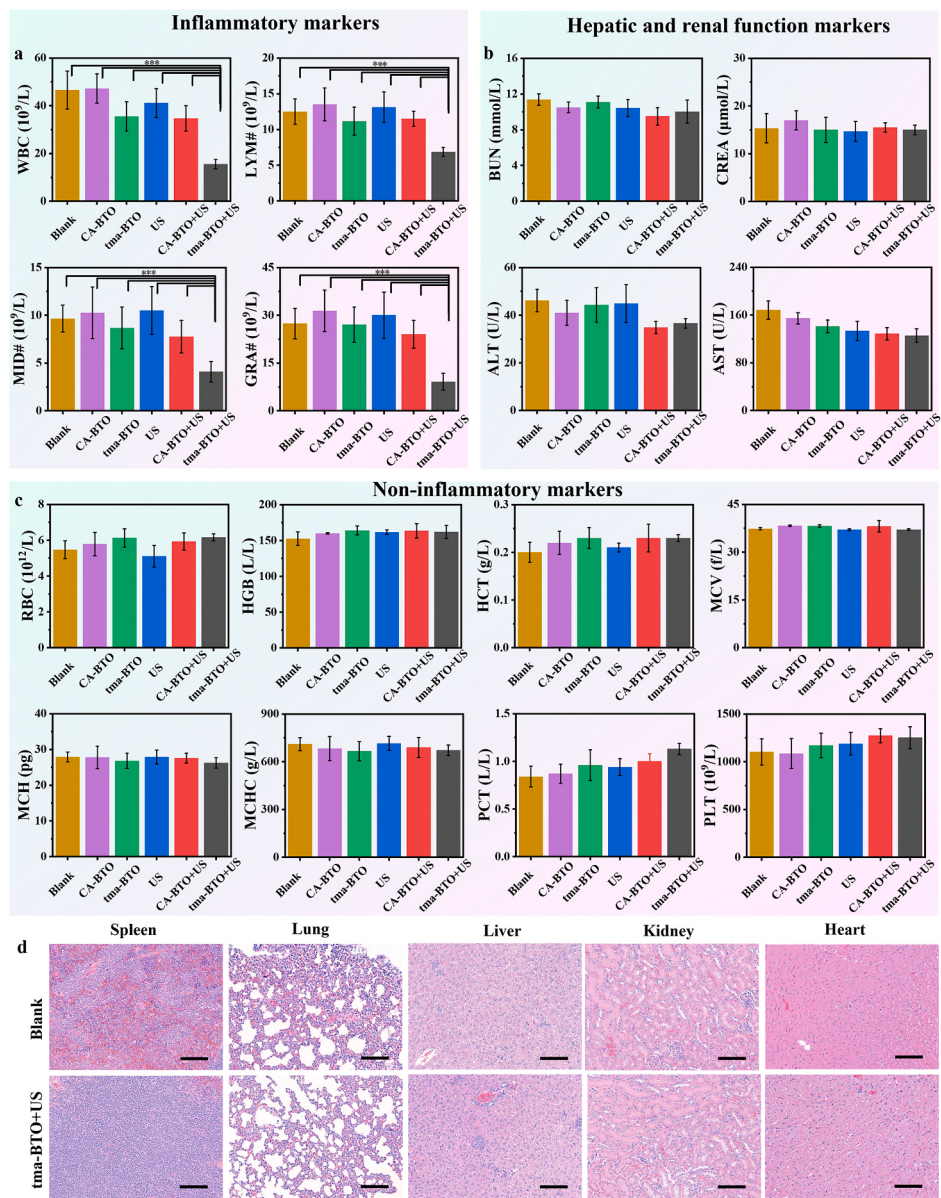


Fig. 6. The biological safety evaluation of the *in vivo* therapeutic performance on female BALB/C mice. Blood biochemistry associated with (a) inflammatory markers, (c) non-inflammatory markers, and (b) hepatic and renal function markers on day 24. (d) H&E assays of heart, liver, spleen, lung, and kidney (Scale bar = 100 μm). (*p < 0.05, **p < 0.01, ***p < 0.001).

perspectives for future piezoelectric-catalyzed precision therapy.

4. Experimental methods

Materials: Sodium hydroxide (NaOH, 99 %), Sodium oleate (97 %), Barium acetate ($\text{Ba}(\text{AC})_2$, 97 %), Tetrabutyl titanate ($(\text{Ti}(\text{Bu})_4$, 99 %), Ethylenediamine solution, Sodium borohydride (99 %), 1-butanol solution, Oleic acid, Toluene, and Ethanol purchased from Aladdin Reagent (Shanghai, China); (\pm)- α - Lipoic acid, 1,1-carbonyldimidazole, and Sodium borohydride were obtained from Sigma-Aldrich. DMEM, CCK-8 Cell Proliferation and Cytotoxicity Assay Kit, Reactive Oxygen Species Assay Kit, and Calcein-AM/PI Assay Kit were acquired from Beijing Solarbio Science & Technology Ltd (China). 1,3-diphenylisobenzofuran (DPBF), terephthalic acid (TA), and methylene blue (MB) were purchased from Shanghai Macklin. All reagents were used directly as received without further purification.

Synthesis of BTO NPs: BaTiO_3 NPs were synthesized using a hydrothermal reaction. In the typical method, $\text{Ba}(\text{AC})_2$ (2.5 ml, 1 mol/L),

NaOH (5.0 ml, 5.0 mol/L), sodium oleate (1.0 g, 97 %), 1-butanol solution (10 mL, 99 %) and 15 mL of oleic acid containing 2.5 mmol $\text{Ti}(\text{Bu})_4$ were added into a 50 ml autoclave tube (160 °C for 12 h). After the reaction was cooled down to room temperature, the products were collected by centrifugation with ethanol and washed with toluene, the purification procedure was repeated three times.

Synthesis of pH-responsive ligands: To prepare the pH-responsive ligands, 1.0 g (\pm)- α -Lipoic acid was dissolved in 6.0 mL of anhydrous chloroform. Then, 1 g 1,1-carbonyldimidazole was added to 1 ((\pm)- α -Lipoic) solution for another 5 min stirring at room temperature. The well-stirred solution was transferred into an ice bath for a while. Then 3.5 mL ethylenediamine solution was added and stirred for 40 min. The crude products were washed three times with saturated NaCl aqueous solution and collected by centrifugation. Subsequently, the solvent was removed using a rotary evaporator to obtain (N-(2-aminoethyl)-5-(1,2-dithiolan-3-yl) pentanamide). Finally, 0.34 mL citraconic anhydride was added dropwise into 7.5 mL of an anhydrous chloroform solution of 2. The solution was stirred overnight at room temperature to

obtain 3 (4-((2-(5-(1,2-dithiolan-3-yl)pentanamido)ethyl)amino)-2-methyl-4-oxobut-2-enoic acid). The synthesized product 0.78 g was dissolved in 15 mL of deionized water, and the solution was adjusted to pH 10 using a 0.01 M NaOH aqueous solution. An equimolar amount of sodium borohydride was added and stirred at room temperature for 30 min. The pH-responsive ligand 4 (4-(2-(6,8-Dimercaptooctanamido)ethylamino)-2-methyl-4-oxobut-2-enoic acid) was eventually obtained, and the color of reaction solution changed from yellow to transparent.

Fabrication of tma-BTO NPs: To fabricate tma-BTO NPs, the prepared BTO NPs were well-dispersed in chloroform solvent, and an equal volume pH-responsive ligand solution (the molar ratio of BTO: pH-responsive ligand = 1: 5) was added and formed the chloroform/water solvent, stirring at 45 °C. After a 4 h reaction, the upper solution was collected and transferred to a new pH-responsive ligand solution. Then, the solution was treated with intense ultrasonication and dialyzed three times using Amicon ultra 100 KDa Mw cutoff centrifugal filters for purification; CA-BTO was synthesized via surface modification [50].

US-triggering piezocatalytic Performance: The $^1\text{O}_2$ radicals generation can be detected by using 1, 3-diphenyl isobenzofuran (DPBF) as a specific probe. 20 μM of DPBF ethanol solution was mixed with 1 mL of BTO aqueous suspension (20 $\mu\text{g/mL}$). Under US irradiation (1.0 MHz, 1.0 W/cm², 50 % duty cycle), the absorption spectra of the mixture were recorded at 411 nm (UV-3600; Shimadzu, Japan). Terephthalic acid (TA) was used as a fluorescent probe to detect $\bullet\text{OH}$ radicals. 0.5 Mm of TA solution was dissolved in a 2 mM NaOH solution. Then CA-BTO (200 $\mu\text{g/mL}$) was added and exposed to US irradiation. The fluorescence intensity of the mixture was measured by a fluorescence spectrophotometer (Edinburgh FLS980 fluorescence spectrophotometer, UK; $\lambda_{\text{ex}} = 315$ nm); Electron spin resonance (ESR) measurements were used for further detecting the $\bullet\text{OH}$ and $^1\text{O}_2$ radicals generation (Bruker E500 ESR spectrometer, USA). 5, 5-dimethyl-1-pyrroline N-oxide (DMPO) and 2, 2, 6, 6-tetramethyl-4-piperidine (TEMP) were adopted as the spin-trapping agents of $\bullet\text{OH}$ and $^1\text{O}_2$ radicals, respectively; The ultrasound irradiation was supported by Intelect Mobile Ultrasound (DJO 2776, American).

In vitro Cytotoxicity Analysis: To evaluate the in vitro biocompatibility of tma-BTO and CA-BTO, CCK-8 Cell Proliferation and Cytotoxicity Assay Kits were used. Briefly, 4T1 cells or MC3T3-E1 cell suspension were seeded in 96-well plates (100 $\mu\text{L}/\text{well}$) at a density of 8×10^3 cells. When cultured overnight, the seed cells are fully attached. Then, the cells were co-cultured with a gradient concentration of tma-BTO or CA-BTO (0, 50, 100, 200, 300, 400, and 500 $\mu\text{g/mL}$; n = 5) in a cell incubator (at 37 °C, 5 % CO₂) for 24 h. After removing the DMEM medium, a fresh DMEM medium was added to the 96-well plates. Then CCK-8 solution (10 $\mu\text{L}/\text{well}$) was carefully added dropwise into and incubated for 1 h. Finally, the microplate reader was used to measure the absorbance at 450 nm.

Calcein-AM/PI Staining: To visualize CCK-8 results, Calcein-AM/PI Staining Reagent was used to stain live/dead cells based on green fluorescence imaging of calcein-AM and red fluorescence imaging of PI. 4T1 cells or MC3T3-E1 cells (1×10^5 cells per well) were incubated in 6-well culture plates with 2 mL DMEM medium (containing 200 $\mu\text{g/mL}$ tma-BTO/CA-BTO) for 24 h co-culture; US irradiation (1.0 MHz, 1.0 W/cm², 50 % duty cycle) was performed for 2 min. Then, the medium was removed and 4T1 cells were stained by adding the mixture (10 $\mu\text{g/mL}$ Calcein-AM and 15 $\mu\text{g/mL}$ PI; PBS) for 30 min. Finally, the mixture was removed and washed with PBS three times, observing the fluorescent signal with a fluorescence microscope (AM $\lambda_{\text{ex}} = 490$ nm, PI $\lambda_{\text{ex}} = 535$ nm; Leica DMI16000B, Germany).

Detection of Intracellular ROS: DCFH-DA assays were used as a fluorescence probe to visualize the intracellular ROS level. 4T1 cells and MC3T3-E1 cells were cultured separately in confocal laser scanning microscopy (CLSM) culture disks (5×10^4 cells per well) for 12 h incubation. Afterward, the DMEM was removed, and each well was added 2 mL DMEM medium (containing 200 $\mu\text{g/mL}$ of tma-BTO or CA-BTO) for 24 h incubation. 4T1 cells or MC3T3-E1 cells were stained with non-

fluorescent DCFH-DA (2 mL, 10 $\mu\text{g/mL}$) for 30 min. Finally, excess DCFH-DA was removed and carefully rinsed three times with PBS; US irradiation (1.0 MHz, 1.0 W/cm², 50 % duty cycle, 2 min) was used to trigger the ROS generation, and the result was recorded by CLSM ($\lambda_{\text{ex}} = 504$ nm; Leica SP8, Germany).

In vivo Tumor Therapy and Evaluation: To BALB/c mice (female, 6 weeks; Vital River, Beijing) were purchased and followed the Beijing Administration Rule of Laboratory Animals. All animal procedures followed the national standards of Laboratory Animal Requirements of Environment and Housing Facilities (GB14925–2001). Then, the mice were injected subcutaneously with 4T1 cells suspension (1×10^6 per mouse, PBS) on the right top thigh. Meantime, the tumor volume and the body weight were recorded every 2 days. When the tumor reached 100–200 mm³, the mice were randomly divided into six groups (n = 6): 1) blank group; 2) US group; 3) CA-BTO group; 4) tma-BTO group; 5) CA-BTO + US group; 6) tma-BTO + US. Subsequently, tma-BTO or CA-BTO (100 μl , 2 mg/100 g body weight) was injected subcutaneously at the peritumoral site. The solid tumor was exposed to US irradiation (1.0 MHz, 1.0 W/cm², 50 % duty cycle; from day 8 to day 16, 3 times a day, each times for 2 min) Finally, blood, solid tumor, and the main organs (heart, liver, spleen, lungs, kidneys) were collected and used for histopathological analysis and the blood biochemistry assay.

Statistical Analysis: Data statistics and statistical significance calculations were conducted using Origin 9.0, Microsoft Excel 2019, and GraphPad Prism 9. All results were expressed as mean \pm s.d. The statistical significance of all data was analyzed using one-way analysis of ANOVA and denoted as *p < 0.05, **p < 0.01, ***p < 0.001.

Data availability

The data that support the findings in this paper are available from the corresponding author upon reasonable request.

Ethics approval and consent to participate

Our study was approved by the ethical committee of the Beijing Institute of Nanoenergy and Nanosystems (A2022057).

CRediT authorship contribution statement

Zhuo Xiang: Data curation, Formal analysis, Investigation, Methodology, Writing – original draft. **Lingling Xu:** Formal analysis, Methodology. **Yizhu Shan:** Formal analysis, Methodology. **Xi Cui:** Formal analysis, Methodology. **Bojing Shi:** Investigation. **Yuan Xi:** Methodology. **Panxing Ren:** Methodology. **Xuemei Zheng:** Formal analysis. **Chaochao Zhao:** Conceptualization, Supervision. **Dan Luo:** Conceptualization, Project administration, Supervision, Writing – review & editing, Funding acquisition. **Zhou Li:** Conceptualization, Funding acquisition, Project administration, Supervision, Writing – review & editing.

Declaration of competing interest

The authors declare that they have no known competing financial interests or personal relationships that could have appeared to influence the work reported in this paper.

Acknowledgments

This work was financially supported by National Key Research and Development Program of China (2022YFE0111700, 2021YFB3201204), the National Natural Science Foundation of China (T2125003, 52372174), the open project of State Drug Administration Key Laboratory of Oral Materials (PKUSS20210401), the Beijing Natural Science Foundation (JQ20038, L212010), the Fundamental Research Funds for the Central Universities, and the Scientific Research Project of

Guangdong Provincial Education Department (2022KTSCX118).

Appendix A. Supplementary data

Supplementary data to this article can be found online at <https://doi.org/10.1016/j.bioactmat.2023.11.004>.

References

- [1] X. Li, J. Song, T. Lin, J. Dixon, G. Zhang, H. Ye, Urbanization and health in China, thinking at the national, local and individual levels, *Environ. Health* 15 (1) (2016) S32.
- [2] R. Zheng, S. Zhang, H. Zeng, S. Wang, K. Sun, R. Chen, L. Li, W. Wei, J. He, Cancer incidence and mortality in China, 2016, *J. Natl. Cancer Cent.* 2 (1) (2022) 1–9.
- [3] E. Boselli, M. Daniela-Ionescu, G. Béguet, L. Bouvet, R. Dabouz, C. Magnin, B. Allaouchiche, Prospective observational study of the non-invasive assessment of immediate postoperative pain using the analgesia/noceotion index (ANI), *Br. J. Addiction: Br. J. Anaesth.* 111 (3) (2013) 453–459.
- [4] Noninvasive treatments for acute, subacute, and chronic low back pain: a clinical practice guideline from the American college of physicians, *Ann. Intern. Med.* 166 (7) (2017) 514–530.
- [5] G. Wei, Y. Wang, X. Huang, H. Hou, S. Zhou, Peptide-based nanocarriers for cancer therapy, *Small Methods* 2 (9) (2018), 1700358.
- [6] Y. Kang, Z. Mao, Y. Wang, C. Pan, M. Ou, H. Zhang, W. Zeng, X. Ji, Design of a two-dimensional interplanar heterojunction for catalytic cancer therapy, *Nat. Commun.* 13 (1) (2022) 2425.
- [7] Y. Meng, Y. Chen, J. Zhu, Y. Qi, J. Ding, W. Zhou, Polarity control of DNA adsorption enabling the surface functionalization of CuO nanozymes for targeted tumor therapy, *Mater. Horiz.* 8 (3) (2021) 972–986.
- [8] K.V. Ramana, S. Srivastava, S.S. Singhal, Lipid peroxidation products in human health and disease, *Oxid. Med. Cell. Longev.* 2013 (2013), 583438.
- [9] L.-J. Su, J.-H. Zhang, H. Gomez, R. Murugan, X. Hong, D. Xu, F. Jiang, Z.-Y. Peng, Reactive oxygen species-induced lipid peroxidation in apoptosis, autophagy, and ferroptosis, *Oxid. Med. Cell. Longev.* 2019 (2019), 5080843.
- [10] Z. Qian, N. Zhao, C. Wang, W. Yuan, Injectable self-healing polysaccharide hydrogel loading CuS and pH-responsive DOX@ZIF-8 nanoparticles for synergistic photothermal-photodynamic-chemo therapy of cancer, *J. Mater. Sci. Technol.* 127 (2022) 245–255.
- [11] M. Fu, Y. Shen, H. Zhou, X. Liu, W. Chen, X. Ma, Gallium-based liquid metal micro/nanoparticles for photothermal cancer therapy, *J. Mater. Sci. Technol.* 142 (2023) 22–33.
- [12] W. Ni, K. Jiang, Q. Ke, J. Su, X. Cao, L. Zhang, C. Li, Development of an intelligent heterojunction fenton catalyst for chemodynamic/starvation synergistic cancer therapy, *J. Mater. Sci. Technol.* 141 (2023) 11–20.
- [13] T. Jin, D. Cheng, G. Jiang, W. Xing, P. Liu, B. Wang, W. Zhu, H. Sun, Z. Sun, Y. Xu, X. Qian, Engineering naphthalimide-cyanine integrated near-infrared dye into ROS-responsive nanohybrids for tumor PDT/PTT/chemotherapy, *Bioact. Mater.* 14 (2022) 42–51.
- [14] L.-S. Lin, J. Song, L. Song, K. Ke, Y. Liu, Z. Zhou, Z. Shen, J. Li, Z. Yang, W. Tang, G. Niu, H.-H. Yang, X. Chen, Simultaneous fenton-like ion delivery and glutathione depletion by MnO₂-based nanoagent to enhance chemodynamic therapy, *Angew. Chem. Int. Ed.* 57 (18) (2018) 4902–4906.
- [15] B. Ma, S. Wang, F. Liu, S. Zhang, J. Duan, Z. Li, Y. Kong, Y. Sang, H. Liu, W. Bu, L. Li, Self-assembled copper-amino acid nanoparticles for in situ glutathione “AND” H₂O₂ sequentially triggered chemodynamic therapy, *J. Am. Chem. Soc.* 141 (2) (2019) 849–857.
- [16] X. Huang, N.T. Blum, J. Lin, J. Shi, C. Zhang, P. Huang, Chemotherapeutic drug-DNA hybrid nanostructures for anti-tumor therapy, *Mater. Horiz.* 8 (1) (2021) 78–101.
- [17] A. Bar-Zion, A. Nourmahnad, D.R. Mittelstein, S. Shivaei, S. Yoo, M.T. Buss, R. C. Hurt, D. Malounda, M.H. Abedi, A. Lee-Gosselin, M.B. Swift, D. Maresca, M. G. Shapiro, Acoustically triggered mechanotherapy using genetically encoded gas vesicles, *Nat. Nanotechnol.* 16 (12) (2021) 1403–1412.
- [18] C. Zhang, L. Xin, J. Li, J. Cao, Y. Sun, X. Wang, J. Luo, Y. Zeng, Q. Li, Y. Zhang, T. Zhang, P. Huang, Metal-organic framework (MOF)-Based ultrasound-responsive dual-sonosensitizing nanoplatform for hypoxic cancer therapy, *Adv. Healthcare Mater.* 11 (2) (2022), 2101946.
- [19] V.G. Deepagan, D.G. You, W. Um, H. Ko, S. Kwon, K.Y. Choi, G.-R. Yi, J.Y. Lee, D. S. Lee, K. Kim, I.C. Kwon, J.H. Park, Long-circulating Au-TiO₂ nanocomposite as a sonosensitizer for ROS-mediated eradication of cancer, *Nano Lett.* 16 (10) (2016) 6257–6264.
- [20] X. Qian, Y. Zheng, Y. Chen, Micro/nanoparticle-augmented sonodynamic therapy (SDT): breaking the depth shallow of photoactivation, *Adv. Mater.* 28 (37) (2016) 8097–8129.
- [21] J. Ji, C. Yang, Y. Shan, M. Sun, X. Cui, L. Xu, S. Liang, T. Li, Y. Fan, D. Luo, Z. Li, Research trends of piezoelectric nanomaterials in biomedical engineering, *Adv. NanoBiomed. Res.* 3 (1) (2023), 2200088.
- [22] C. Yang, J. Ji, Y. Lv, Z. Li, D. Luo, Application of piezoelectric material and devices in bone regeneration, *Nanomaterials* 12 (24) (2022) 4386.
- [23] W. Qian, W. Yang, Y. Zhang, C.R. Bowen, Y. Yang, Piezoelectric materials for controlling electro-chemical processes, *Nano-Micro Lett.* 12 (1) (2020) 149.
- [24] X. Yan, G. Li, Z. Wang, Z. Yu, K. Wang, Y. Wu, Recent progress on piezoelectric materials for renewable energy conversion, *Nano Energy* 77 (2020), 105180.
- [25] X. Zhou, B. Shen, A. Lyubartsev, J. Zhai, N. Hedin, Semiconducting piezoelectric heterostructures for piezo- and piezophotocatalysis, *Nano Energy* 96 (2022), 107141.
- [26] L. Chen, Z. Mao, Y. Wang, Y. Kang, Y. Wang, L. Mei, X. Ji, Edge modification facilitated heterogenization and exfoliation of two-dimensional nanomaterials for cancer catalytic therapy, *Sci. Adv.* 8 (39) (2022), eabo7372.
- [27] H. Zhang, H. Gao, J. Geng, X. Meng, H. Xie, In situ quantification of strain-induced piezoelectric potential of dynamically bending ZnO microwires, *Small Methods* 7 (3) (2023), 2201342.
- [28] H. Li, L. Zhao, J. Meng, C. Pan, Y. Zhang, Y. Zhang, Z. Liu, Y. Zou, Y. Fan, Z. L. Wang, Z. Li, Triboelectric-polarization-enhanced high sensitive ZnO UV sensor, *Nano Today* 33 (2020), 100873.
- [29] G.-J. Lee, M.-K. Lee, J.-J. Park, D.Y. Hyeon, C.K. Jeong, K.-I. Park, Piezoelectric energy harvesting from two-dimensional boron nitride nanoflakes, *ACS Appl. Mater. Interfaces* 11 (41) (2019) 37920–37926.
- [30] G. Ciofani, S. Danti, D. D'Alessandro, L. Ricotti, S. Moscato, G. Bertoni, A. Falqui, S. Berrettini, M. Petrini, V. Mattoli, A. Menciassi, Enhancement of neurite outgrowth in neuronal-like cells following boron nitride nanotube-mediated stimulation, *ACS Nano* 4 (10) (2010) 6267–6277.
- [31] X. Liang, X. Yu, L. Lv, T. Zhao, S. Luo, S. Yu, R. Sun, C.-P. Wong, P. Zhu, BaTiO₃ internally decorated hollow porous carbon hybrids as fillers enhancing dielectric and energy storage performance of sandwich-structured polymer composite, *Nano Energy* 68 (2020), 104351.
- [32] Y. Zhao, S. Wang, Y. Ding, Z. Zhang, T. Huang, Y. Zhang, X. Wan, Z.L. Wang, L. Li, Piezotronic effect-augmented Cu₂-xO-BaTiO₃ sonosensitizers for multifunctional cancer dynamic therapy, *ACS Nano* 16 (6) (2022) 9304–9316.
- [33] J.P. Ball, B.A. Mound, J.C. Nino, J.B. Allen, Biocompatible evaluation of barium titanate foamed ceramic structures for orthopedic applications, *J. Biomed. Mater. Res.* 102 (7) (2014) 2089–2095.
- [34] T. Jordan, M.A. O'Brien, C.-P. Spatarelu, G.P. Luke, Antibody-conjugated barium titanate nanoparticles for cell-specific targeting, *ACS Appl. Nano Mater.* 3 (3) (2020) 2636–2646.
- [35] G.G. Genchi, A. Marino, A. Rocca, V. Mattoli, G. Ciofani, Barium titanate nanoparticles: promising multitasking vectors in nanomedicine, *Nanotechnology* 27 (23) (2016), 232001.
- [36] C. Li, C. Xiao, L. Zhan, Z. Zhang, J. Xing, J. Zhai, Z. Zhou, G. Tan, J. Piao, Y. Zhou, S. Qi, Z. Wang, P. Yu, C. Ning, Wireless electrical stimulation at the nanoscale interface induces tumor vascular normalization, *Bioact. Mater.* 18 (2022) 399–408.
- [37] G. Jin, Z. Gao, Y. Liu, J. Zhao, H. Ou, F. Xu, D. Ding, Polymeric nitric oxide delivery nanoplatforms for treating cancer, cardiovascular diseases, and infection, *Adv. Healthcare Mater.* 10 (3) (2021), 2001550.
- [38] M. Sousa de Almeida, E. Susnik, B. Drasler, P. Taladriz-Blanco, A. Petri-Fink, B. Rothen-Rutishauser, Understanding nanoparticle endocytosis to improve targeting strategies in nanomedicine, *Chem. Soc. Rev.* 50 (9) (2021) 5397–5434.
- [39] X. Wan, H. Zhang, Q. Yan, H. Hu, W. Pan, Y. Chai, Y. Gao, N. Li, B. Tang, Three-dimensional covalent organic frameworks as enzyme nanoprotector: preserving the activity of catalase in acidic environment for hypoxia cancer therapy, *Mater. Today Nano* 19 (2022), 100236.
- [40] G.-B. Ding, C. Zhu, Q. Wang, H. Cao, B.-C. Li, P. Yang, R.H. Stauber, G. Nie, Z. Li, Molecularly engineered tumor acidity-responsive plant toxin gelonin for safe and efficient cancer therapy, *Bioact. Mater.* 18 (2022) 42–55.
- [41] G. Li, J. Sun, W. Hou, S. Jiang, Y. Huang, J. Geng, Three-dimensional porous carbon composites containing high sulfur nanoparticle content for high-performance lithium-sulfur batteries, *Nat. Commun.* 7 (1) (2016), 10601.
- [42] S. Wang, X. Wang, S. Feng, W. Lv, M. Lin, Q. Ling, Z. Lin, Cluster-luminescent polysiloxane nanomaterials: adjustable full-color ultralong room temperature phosphorescence and a highly sensitive response to silver ions, *Inorg. Chem. Front.* 9 (14) (2022) 3619–3626.
- [43] S. Kang, S.H. Bhang, S. Hwang, J.-K. Yoon, J. Song, H.-K. Jang, S. Kim, B.-S. Kim, Mesenchymal stem cells aggregate and deliver gold nanoparticles to tumors for photothermal therapy, *ACS Nano* 9 (10) (2015) 9678–9690.
- [44] J. Nam, N. Won, H. Jin, H. Chung, S. Kim, pH-induced aggregation of gold nanoparticles for photothermal cancer therapy, *J. Am. Chem. Soc.* 131 (38) (2009) 13639–13645.
- [45] T. Nie, W. Zou, Z. Meng, L. Wang, T. Ying, X. Cai, J. Wu, Y. Zheng, B. Hu, Bioactive iridium nanoclusters with glutathione depletion ability for enhanced sonodynamic-triggered ferroptosis-like cancer cell death, *Adv. Mater.* 34 (45) (2022), 2206286.
- [46] P. Wang, Q. Tang, L. Zhang, M. Xu, L. Sun, S. Sun, J. Zhang, S. Wang, X. Liang, Ultrasmall barium titanate nanoparticles for highly efficient hypoxic tumor therapy via ultrasound triggered piezocatalysis and water splitting, *ACS Nano* 15 (7) (2021) 11326–11340.
- [47] A. Marino, M. Battaglini, D. De Pasquale, A. Degl'Innocenti, G. Ciofani, Ultrasound-activated piezoelectric nanoparticles inhibit proliferation of breast cancer cells, *Sci. Rep.* 8 (1) (2018) 6257.
- [48] C. Pucci, A. Marino, Ö. Sen, D. De Pasquale, M. Bartolucci, N. Iturrio-Rodríguez, N. di Leo, G. de Vito, D. Debelle, A. Petretto, G. Ciofani, Ultrasound-responsive nutlin-loaded nanoparticles for combined chemotherapy and piezoelectric treatment of glioblastoma cells, *Acta Biomater.* 139 (2022) 218–236.
- [49] Y. Wu, X. Song, X. Zhou, R. Song, W. Tang, D. Yang, Y. Wang, Z. Lv, W. Zhong, H.-L. Cai, A. Zhang, J. Wei, X.S. Wu, Piezo-activated atomic-thin molybdenum disulfide/MXene nanoenzyme for integrated and efficient tumor therapy via ultrasound-triggered Schottky electric field, *Small* 19 (9) (2023), 2205053.
- [50] R.H. Huang, N.B. Sobol, A. Younes, T. Mamun, J.S. Lewis, R.V. Ulijn, S. O'Brien, Comparison of methods for surface modification of barium titanate nanoparticles for aqueous dispersibility: toward biomedical utilization of perovskite oxides, *ACS Appl. Mater. Interfaces* 12 (46) (2020) 51135–51147.